Study about the influence of an automatic meshing algorithm on numerical simulations of a Gaseous-Fueled Lean Direct Injection (LDI) Gas Turbine Combustor in Non-Reactive conditions

Payri, R.[1], Novella, R.[1], Carreres, M.*[1], Belmar-Gil[1]
[1]CMT-Motores Térmicos, Universitat Politècnica de València, 46022 Valencia, Spain
*Corresponding author: marcarta@mot.upv.es

Abstract
Aeronautical gas turbine engines present the main challenge of increasing their efficiency while keeping the pollutant emissions below strict limits. Numerical CFD simulations of these devices are usually computationally unaffordable since they imply a multi-scale problem. In this investigation, a non-premixed natural gas lean-direct-injection burner is simulated though U-RANS and LES in non-reactive conditions. The geometry considered is the gaseous configuration of the CORIA academic burner, for which quality validation data is available. Fuel is directly injected in the combustion chamber and surrounded by air from a radial swirler corresponding to a global equivalence ratio of 0.75. This work focuses on investigating the impact of an Adaptive Mesh Refinement algorithm in the accuracy and the computational cost through the evaluation of U-RANS simulations and its application to LES in predicting the flow recirculation zones and the fuel-air mixing degree generated within the combustor. Results show a good agreement of U-RANS and LES with AMR in capturing time-averaged velocity profiles compared against experimental data. Meanwhile, LES demonstrate more accurate predicted results in terms of fluctuations and a greater ability to capture the unsteady fluid dynamic structures, as expected.

Keywords
Gas turbine combustor, Swirling flow, Large Eddy Simulation, Adaptive Mesh Refinement, Non-reactive flow.

Introduction

Aeronautical gas turbine engines present the main challenge of increasing the efficiency of the cycle while keeping the pollutant emissions below stringent restrictions [1]. This has led to the design of new injection-combustion strategies working on more risky and problematic operating points such as those close to the lean extinction limit. In this context, the Lean Direct Injection (LDI) concept has emerged as the most promising technology to reduce oxides of nitrogen (NOx) for next-generation aircraft gas turbine engines [2]. In LDI combustors, fuel is directly injected in the combustion chamber and surrounded by an incoming swirling airstream. Hence, atomization, fuel-air mixing, ignition, and flame propagation occur at an equivalence ratio close to the lower flammability limit downstream the injection system, where a high-turbulent recirculation zone is generated as a result of the existing swirling vortex flow. Even though the main interest of the LDI burners reside on liquid-fueled systems, lean swirl-stabilized combustion is extensively used in premixed and non-premixed gaseous academical systems as well [3]. Swirling flows are employed in most engine designs, but its chaotic nature hinders both experimental measurements and numerical computations. Even though a significant effort has been made on investigating the swirling flow in gas turbine combustors [4-6], some processes remain a challenge for both experiments and simulations. On the one hand, experimental observation of spray breakup, mixing, and combustion in swirling flows still present some challenges concerning uncertainties in getting an accurate prediction in the dense regime [7]. Furthermore, phenomena such as flame stability and engine re-ignition in altitude remain a substantial challenge for designers. On the other hand, a vast number of computational researches of swirling spray combustors have been carried out. Given the high turbulence level and unsteady structures generated by the swirling motion inside the combustion chamber, the Unsteady Reynolds-Averaged Navier Stokes (U-RANS) turbulence modeling approach precludes a complete analysis of the robust oscillations [8], failing in predicting turbulence fluctuation statistics. Recently, some direct numerical simulation (DNS) investigations of swirling spray combustion have been performed [9] in which all the length scales co-existing within the combustor are solved. Nevertheless, the expensive computational cost associated with DNS limits these simulations to low Reynolds numbers so far discarding its viability in engineering applications. In this context, Large Eddy Simulations (LES) emerges as the natural alternative and is considered to be the next-generation numerical design tool for investigating the generation and evolution of coherent structures in swirl-stabilized gas turbine combustors [10-11].

In this study, a series of numerical investigations have been performed using both U-RANS and LES techniques of a gaseous-fueled radial-swirled lean-direct injection (LDI) combustor. The geometry considered is the gaseous configuration of the CORIA Burner, for which detailed measurements are available [12]. The present investigation

addresses the impact of an Adaptive Mesh Refinement algorithm in the accuracy and the computational cost through the evaluation of U-RANS simulations and its extension to LES to overcome U-RANS limitations in resolving the spatial-temporal scales and the intrinsically unsteady flow structures (i.e., vortex breakdown bubble and precessing vortex core) generated within the combustor.

Experimental setup

The experimental LDI burner configuration [12] consists of four main components, depicted in the left side of Figure 1. The combustor employs a radial swirler, illustrated in the right side of Figure 1, composed of 18 channels (6x8mm) inclined at 45º and an external annular swirling air co-flow with an inner and outer diameter of 9 and 20 mm respectively. This swirling air flow enters the square-cross combustion chamber (100x100x260mm), where gaseous methane is injected through a tube (d = 4 mm) acting as the fuel injector located in the center of the swirler.

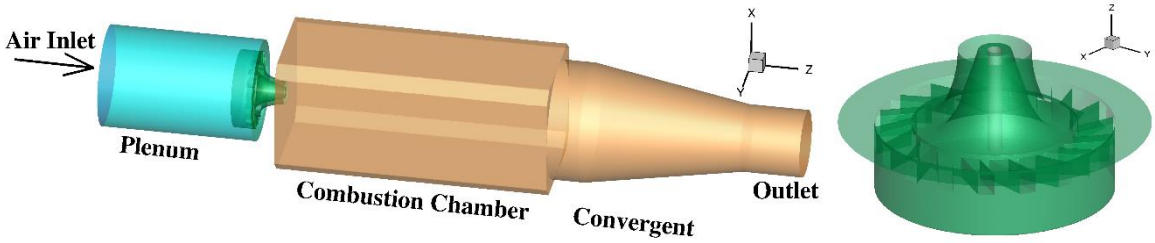

Figure 1. Left: Overview of the CORIA single burner computational domain: the air plenum, the swirl-injection system, the combustion chamber, and the convergent exhaust. Right: Zoom to the swirl-injection system.

In this work, a non-premixed gaseous injection strategy has been simulated at ambient conditions (T = 298 K; p = 1 atm). The operating condition corresponds to a global equivalence ratio of 0.75, where the swirler is fed with 5.43 g/s of air whereas a methane mass flow rate of 0.234 g/s is imposed through the central jet, simulating the experimental conditions reported in [12]. The air enters the combustion chamber as a turbulent jet at a bulk velocity of 27 m/s with significant swirling motion, giving rise to a Reynolds number of 33,000 based on the mean diameter of the convergent inlet. Finally, experimental data have been acquired for velocity (mean and fluctuation) at discrete locations along both the centreline and the three streamwise locations represented in the left side of Figure 2.

Numerical Setup

The computational domain includes the four components of the experimental test rig, as reported in Figure 1 (left). The axial direction is referred to as the z-axis, corresponding to the main flow direction, while the x-axis and y-axis denote the transverse directions.

The CONVERGE™ CFD software [13] is used in the current study to optimize the computational resources in this kind of multi-scale problem utilizing several grid control tools, including adaptive mesh refinement (AMR). The code uses an innovative modified cut-cell Cartesian method that eliminates the need for the computational grid to be morphed with the geometry of interest, while still precisely representing the exact boundary shape. This approach allows for the use of simple orthogonal grids and completely automates the mesh generation process.

In the present solver, all computed values are collocated at the center of the computational cell, where the conservation equations are solved using the finite volume method. A 2nd order spatial discretization scheme is used for both the governing conservation equations and the time accuracy. The Rhie-Chow algorithm is employed to prevent spurious oscillations (e.g., checker-boarding). Meanwhile, the transport equations are solved using the PISO algorithm. A variable time-stepping algorithm is used in the study, where the time-step is automatically calculated each computational cycle based on a maximum allowed CFL value of 0.8.

An automatic domain decomposition technique is employed, allowing for efficient load balancing throughout the calculation. For illustrating purposes, Figure 2 (right) shows the meshing strategy followed through the available grid-tools in CONVERGE^{TM}: the Fixed Embedding, that refines the grid at user-specified locations (areas) and times where a finer resolution is critical to the accuracy of the solution, and the Adaptive Mesh Refinement, which automatically adds embedding where the flow field is more under-resolved, and the velocity gradients between adjacent cells exceed a given user-defined threshold. Both fixed embedding and Adaptive Mesh Refinement were employed to refine the base mesh by cutting the cell dimensions in half for each level of refinement.

The influence of the grid control tools is analyzed for several mesh layouts varying the base mesh size, fixed embedding size and levels, and AMR threshold and levels to obtain a meshing strategy that allows optimizing the available computational resources. For this mesh study, the Standard k-ε turbulence model is employed since fewer cell count, and faster simulations are expected.

Once the strategy is defined, it is applied for the evaluation of the turbulence models. U-RANS (i.e., the Standard k-ε and the LRR Reynolds Stress Model) and LES (i.e., dynamic Smagorinsky) modeling options for the treatment of turbulence have been applied separately to characterize the unsteady non-reacting flow field. Meanwhile,

standard law of the wall profile is used to determine the tangential components of the stress tensor at the wall in U-RANS simulations, whereas the recommended Werner and Wengle [13] wall model is considered in LES.
The resultant mesh strategy leads to a base mesh size for the combustor of 0.15D in all three dimensions for U-RANS (0.1D is used for LES), where D is the external swirl cup exit diameter, defined previously. One layer with one level of fixed embedding was applied over every surface of the combustor for U-RANS (two layers with two levels for LES). Three levels of fixed embedding were also used in the swirler and the entrance of the combustion chamber (see right side of Figure 2). Meanwhile, three levels of AMR were employed to capture regions of high-velocity gradients. Additionally, AMR of y^+ was used to maintain the proper level of mesh near the wall ensuring y^+ values between 30 and 100. These combinations of grid tools together with the particular response of each turbulence model to the AMR algorithm leads to grid mean numbers of cells of 1,300,000 for Standard k-ε, 2,800,000 for LRR RSM, and 14,500,000 for dynamic Smagorinsky LES, as will be shown.

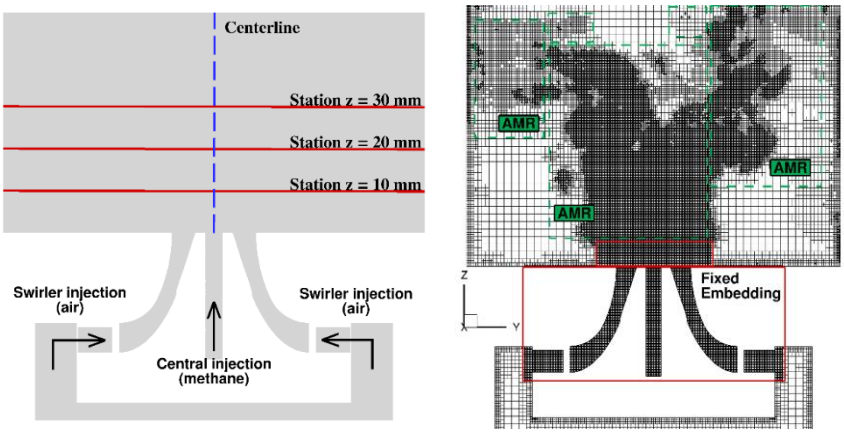

Figure 2. Left: Overview of the measurement transverse cross-section where experimental data are available for comparison with CFD simulations: the centreline, and the radial stations located at three different axial positions. Right: Slice in the computational domain for a LES simulation in CONVERGE™ illustrating the strategy considered in the mesh refinement: 3 levels of fixed embedding, 3 levels of AMR, and 2 layers with 2 levels of wall refinement.

Finally, the flow field was established during the first 50 ms through a mesh scaling of twice the baseline mesh size. Then, the grid was automatically scaled down to recover the base mesh size, and the fixed embedding and AMR tools started to work. The simulations were run for additional 150 ms to stabilize the overall mass flow rate and velocity fields with the final mesh strategy. Afterward, time-averaged runs to compute turbulent statistics (mean and fluctuations of the velocity components, and the mass fuel fraction) were conducted over 100 ms.

Quantifying the accuracy of a simulation

The accuracy of a given simulation is measured through the calculation of the Normalized Mean Square Error (from now on referred to as *NMSE*), defined by Eq. (1):

$$NMSE = \frac{(\phi_N - \phi_E)^2}{|\phi_N \cdot \phi_E|} \tag{1}$$

where ϕ_N is the numerical mean (time-averaged) or RMS value of a given flow variable calculated through CFD in a given spatial location, whereas ϕ_E denotes the same flow variable value obtained experimentally in the same location. A perfect model would have *NMSE* = 0. Despite the quality acceptance criteria for this metric strongly depends on what the data underlying represents, reference studies [14] states *NMSE* < 4 as an acceptable quality criterion for a predictive model. Nevertheless, in this study, the computed *NMSE* value is just utilized to compare the performance between different simulations, and no quality criterion is considered. The strategy followed to evaluate the prediction quality of a given CFD simulation is to obtain three differentiated NMSE values: one for the time-averaged axial velocity along the centerline (i.e., *NMSE-Centerline*), another for the mean of the time-averaged components velocity in all the stations (i.e., *NMSE-Mean-Stations*) and a last one for the same but considering the RMS values (i.e., *NMSE-RMS-Stations*). These three global values are obtained by averaging the discrete values obtained at each discrete location where experimental data is available.
A set of 12 simulations has been performed to analyze the base size influence together with the fixed embedding and AMR is summarized in the left side of Figure 3, for which the *NMSE-Mean-Stations* value is represented. The lines join simulations that keep all the parameters constant (i.e., a given zone of influence and levels of fixed embedding, and a given threshold and levels of AMR) except for the base size, showing the combination of grid tools that allow reducing the number of cells while maintaining the accuracy. Then, the optimal mesh resulting is

applied for the evaluation of the turbulence models previously stated (right side of Figure 3), confirming the ability of LES capturing the unsteadiness of the flow more reliably.

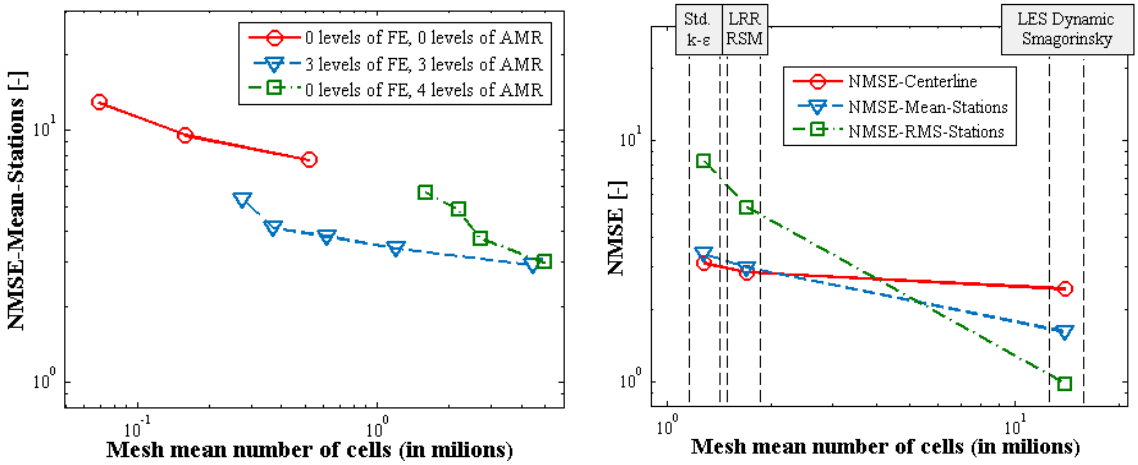

Figure 3. Left: Influence of the grid control tools on the *NMSE-Mean-Stations* value for Standard k-ε simulations. Each line represents the variation of the base size for a given strategy of AMR and fixed embedding refinement. Right: Influence of the turbulence models on the *NMSE-Centerline*, *NMSE-Mean-Stations*, and *NMSE-RMS-Stations* values.

Results and discussion

Flow dynamics

An analysis of the flow dynamics in the combustor and a close examination of the strong turbulent flow near the injection system is carried out in the present section. Results presented in this section are focused on the LES case since it has exhibited the highest accuracy through the comparison of the mean and fluctuation velocity components against the experimental data, as shown through the Agreement Factor in the previous section.

The degree of mixing among the fuel and air in the combustion zone depends mainly on the swirl intensity, usually determined by the swirl number *S* [15], defined as the ratio of the axial flux of the tangential momentum to the product of the axial momentum flux and a characteristic radius:

$$S = \frac{1}{R_{ext}} \frac{\int_{R_{inn}}^{R_{ext}} uwr^2 dr}{\int_{R_{inn}}^{R_{ext}} u^2 r dr} \tag{2}$$

The swirl number in the dump plane of the combustion chamber evaluated through Eq. (2) is 0.79. When *S* exceeds a critical value of 0.6 in the swirler outlet region [16], a phenomenon known as Vortex Breakdown Bubble (VBB) occurs, assisting in the formation of a Central Toroidal Recirculation Zone (CTRZ). Figure 4 (left) shows the streamlines of the time-mean flow field based on the axial velocity in a central *x*-cut plane allowing to illustrate the characteristic flow structures that are typically observed in a gas turbine combustor [17]. The most important is the CTRZ, characterized by energetic turbulence intensity and reverse flow. Moreover, the Corner Recirculation Zones (CRZ) and strong Shear Layers (high shear stresses) originated from the outer edge of the inlet annulus are also shown. The swirl intensity influences all these unsteady 3D flow field features and plays a crucial role in the fuel-air mixing and the flame stabilization mechanism.

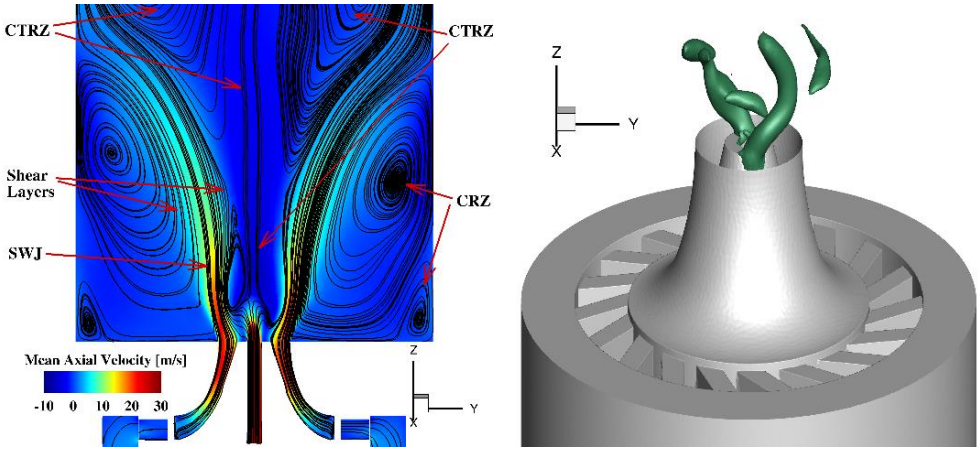

Figure 4. Left: Mean (time-averaged) axial velocity field in a central *x*-cut plane and streamlines patterns showing the characteristic flow pattern within the CORIA LDI Combustor. Right: Instantaneous visualization of the Precessing Vortex Core identified through an isobaric surface with *p* = 101.05 kPa at 275 ms.

The structure of the Precessing Vortex Core (PVC), located surrounding the central recirculation zone, and developed when the central vortex core starts precessing around the combustor axis of symmetry is well captured by LES (see right side of Figure 4). The PVC can be visualized through an isobaric surface of the instantaneous pressure field. It can be defined as a three-dimensional unsteady asymmetric flow structure around the central axis, which tends to align with it near the inlet. Nevertheless, when it reaches the stagnation point of the recirculation zone (i.e., the first zero axial velocity point along the central axis in the left side of Figure 4), it is driven away from the centreline and forms a spiral pattern further downstream in the axial direction. The image exhibits two rotating helicoidal branches ejected from inside the swirler which enter the chamber and are reoriented by the mean rotating flow. These coherent structures strongly affect flow and flame evolution. In fact, the flame front can be affected by the highly turbulent aerodynamic stretching caused by the PVC, thus leading to local quenching or extinction.
The high intensity of turbulence in the CTRZ is demonstrated by the visualization of the Q-criterion captured by LES in Figure 5 (left), which defines vortices as areas where the vorticity magnitude is greater than the magnitude of rate-of-strain. As the flow expands from the swirler exit and evolves downstream, strong shear layers are developed from the large velocity difference between the jet flow and the ambient fluid. Furthermore, the presence of swirl generates an azimuthal shear layer and centrifugal instabilities when the circulation decreases in the outward direction. In this regard, well-organized large vortical structures, arising from the shear layers downstream of the dump plane (illustrated in the left side of Figure 5), are convected downstream, and then become disordered and dissipated into small-scale eddies due to the strong CTRZ. In fact, the CTRZ was found to intersect with the outer shear layer, setting a complex flow field near the injector exit.

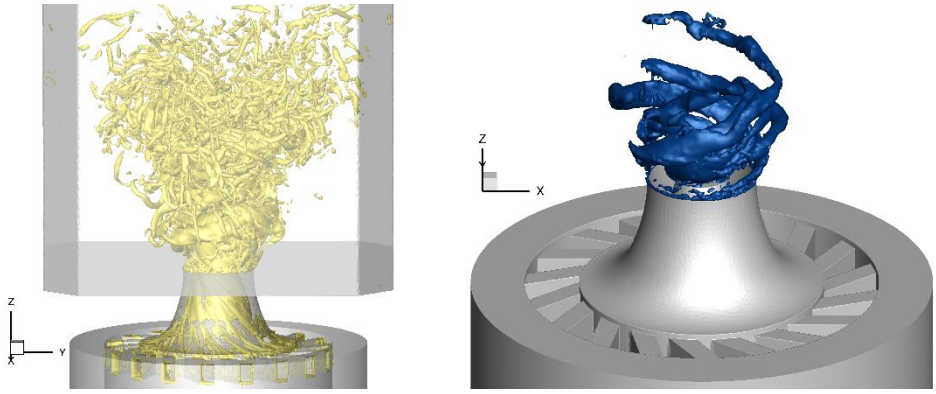

Figure 5. Left: Instantaneous iso-Q criterion ($Q = 10^7$) in the swirler and the combustor at 275 ms. Right: Instantaneous iso-surface of tangential vorticity component (15000 s^{-1}) through the combustion chamber at 275 ms.

To end with the transient analysis, Figure 5 (right) shows a snapshot of an instantaneous positive tangential vorticity iso-surface. The flow field in the region $r > 15$ mm is blanked to provide a clearer picture of the spiral vortex structure. The evolution of these spiral vortex structures can be understood as a kind of vortex shedding with well-defined frequencies closed to the rotation time scale of the PVC. Therefore, the combined axial and tangential shear layers become unstable due to the swirl motion and evolve to a modified form of the Kelvin-Helmholtz (K-H) instability. In this kind of strong swirl flow, vorticity in the tangential shear layer (shown in the right side of Figure 5), generated by the azimuthal velocity, grow and become comparable with the vorticity in the axial shear layer (not shown for clarity). Thus, this joint action of stretch/strain forces the swirling flow to evolve in the axial and azimuthal directions continuously. The aforementioned displacement of the vortex core congestions the flow at one side against the combustor wall, leading to a considerable increase in the tangential velocity in the squeezed flow region due to the conservation of angular momentum. The existence of the PVC also explains the occurrence of instantaneous tangential velocity near the centerline of the combustor.

Mean Features

The statistically averaged flow field allows comparing numerical and experimental velocity profiles. Time-averaged mean and RMS fields of the axial and tangential velocity components in the central x-normal plane are depicted in Figure 6 (zero-axial velocity regions are highlighted in black to clarify the recirculation zones). The high tangential velocity component confirms the strong swirl number, calculated by Eq. (2), of the injection system at the dump plane reaching values as high as those obtained for the axial component. The distributions of the RMS velocity components illustrate the flapping motion of the central jet and SWJ indicating that a high turbulence-intensity region (large velocity fluctuations) is developed at the combustion chamber inlet.
Figures 7 show radial profiles ($x = 0$ corresponds to the centerline of the chamber) of the time-averaged streamwise and tangential mean and fluctuating (RMS) velocity at the three axial locations represented in the right side of Figure 2 ($z = 10$, 20, and 30 mm) within combustion chamber for U-RANS (Standard k-ε and LRR Reynolds Stress Model)

and LES (dynamic Smagorinsky). The computed mean velocity profiles obtained by the three turbulence approaches (left side of figures) show an overall quantitative agreement compared with experimental data throughout the three stations. The global flow topology and the amplitude velocity profiles (both mean and RMS) are reasonably well reproduced. Both the U-RANS and the LES seem to accurately capture the jet opening angle, denoted by the peaks of the mean velocity components around x = 10 mm. The mean axial velocity peak observed at the location z = 10 mm in Figure 7 (top) flattens out as the flow reaches stations far away from the dump plane due to the expansion of the recirculation zone in the central region. Meanwhile, the computed mean axial velocity magnitude at z = 10 mm indicates a stronger penetration of the methane jet at x = 0 (more pronounced in U-RANS), which appreciably moves downstream along the centerline the location of the stagnation point. This discrepancy might be, besides numerical reasons, due to the difficulty in obtaining experimental data at this location, as reported for similar geometries [18]. Profiles also show the negative axial velocities in the central and corner regions, confirming the existence of recirculation zones. Otherwise, the turbulent velocity is lightly under-predicted in the U-RANS simulations (more evident when considering k-ε model) since the governing equations are ensemble-averaged before being solved and the isotropic turbulence hypothesis is assumed, meaning few fluctuations. Profiles are observed to become progressively uniform downstream the entrance of the combustion chamber, indicating rapid 3D mixing. Finally, a quantitative remark through the AF values reported along the stations confirms the greater ability of the dynamic Smagorinsky LES to capture all the time-averaged and turbulent velocity components.

As stated earlier, the additional tangential velocity component imposed in high swirling flows (with its corresponding increase in the Reynolds number for a given mass flow) compared to non-swirling flows enhance the mixing of fuel and oxidizer since the turbulent mixing is increased. Fuel injection and optimal level of mixing among the air and fuel are critical to achieving efficient and low-emission combustion in the engine. The excellent mixing properties of the present combustor are illustrated through the mean and RMS mixture fraction (Z) fields in Figure 8. The presence of the PVC results in periodic perturbation of the local mixture fraction. Results reveal the low penetration of the pure methane (injected through the central jet) far downstream in the chamber, which is quickly mixed in the first axial stations. Meanwhile, most of the combustion chamber is filled with a lean mixture close to the global equivalence ratio of 0.75, corresponding to Z = 0.042.

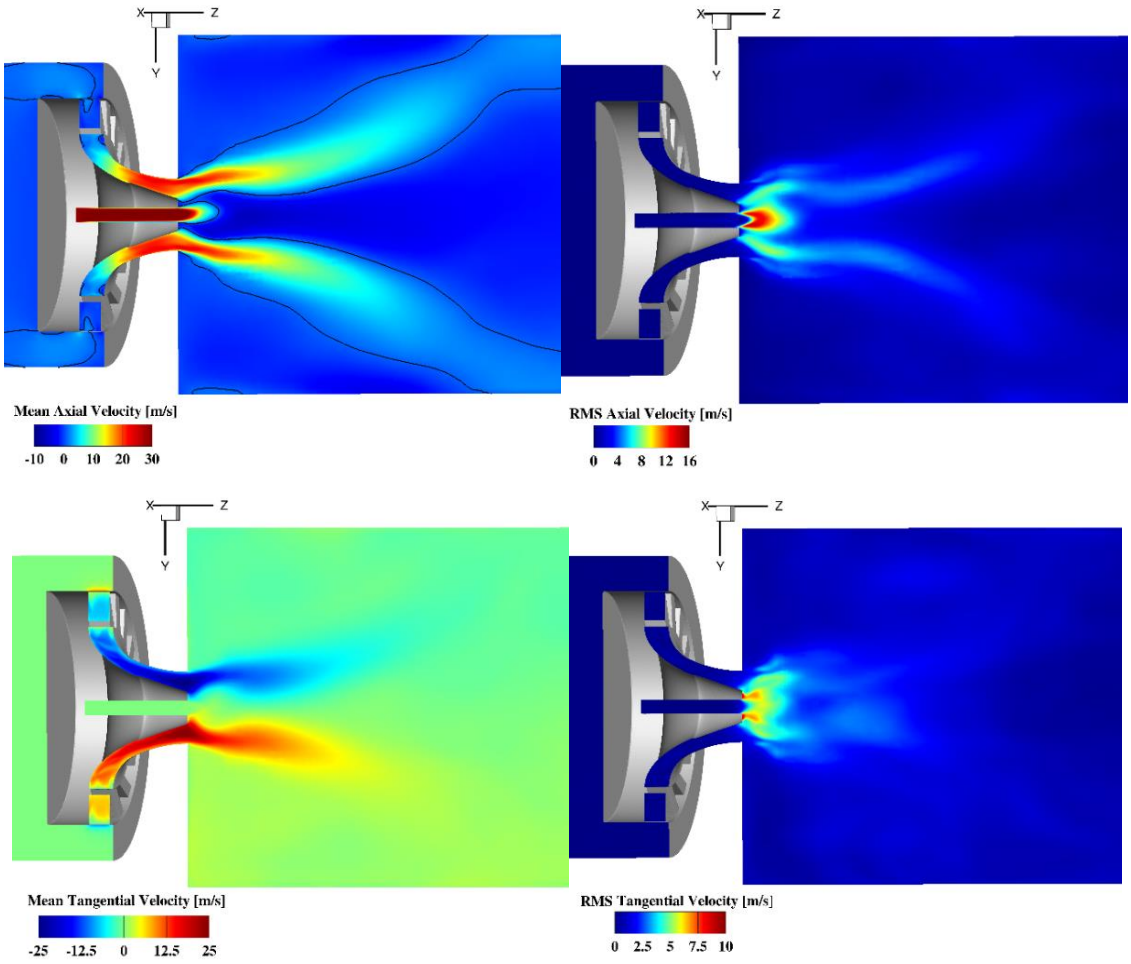

Figure 6. Mean (time-averaged) and RMS velocity components in a central x-cut plane through the combustion chamber in LES.

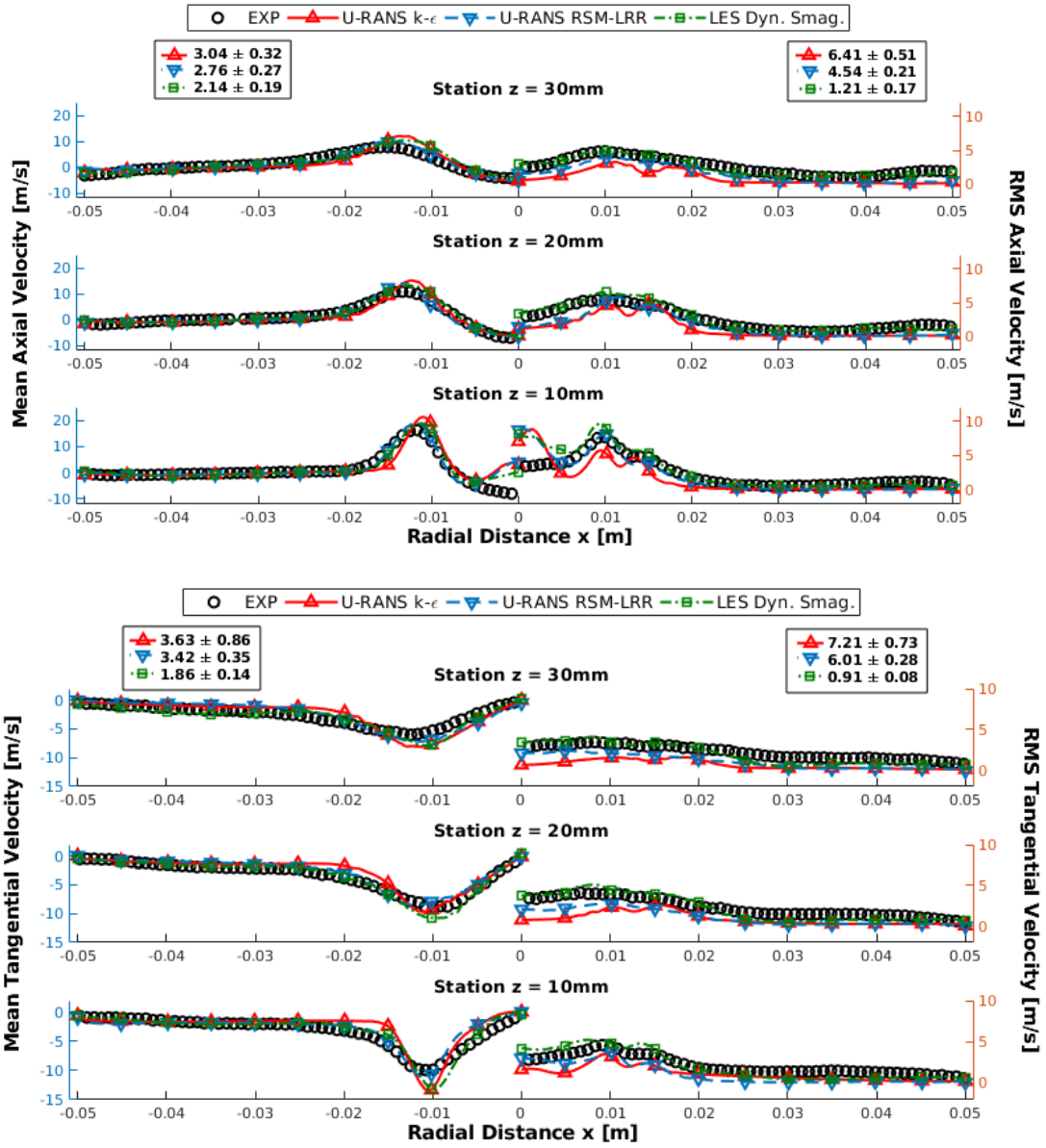

Figure 7. Mean and RMS Axial (Top) and Tangential (Bottom) Velocity profiles obtained in U-RANS and LES simulations at 3 axial locations. The mean NMSE values and its standard deviation between stations are reported for each simulation.

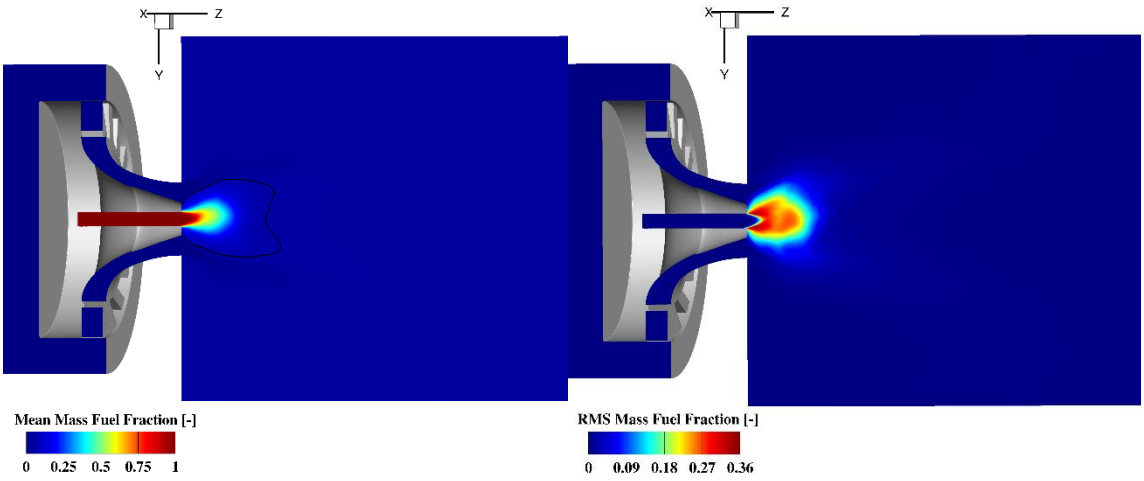

Figure 8. Mean (left), and RMS (right) fuel mass fraction in a central *x*-cut plane through the combustion chamber. The stoichiometric mean mixture fraction (Z_{st} = 0.055) is highlighted in black.

Conclusions

U-RANS and LES simulations have been performed to investigate the non-reactive swirling flow features in a laboratory-scale research combustor with non-premixed gaseous injection. An optimal mesh strategy has been derived, leading to an optimization of the computational resources and allowing to represent detailed turbulent structures. The AMR algorithm has allowed to tackle this multi-scale problem, capturing the critical regions of high-velocity gradients and enabling a larger base mesh size in regions where it was not required. The LES vortex-stretching mechanism have been shown to overcome U-RANS limitations capturing the dynamic behaviour of the flow field and allowing a comprehensive description of the inherently unsteady large structures formed within the combustor, such as the VBB and the PVC. These coherent structures, located in the inner and outer shear layers, result in periodic fluctuations of the local mixture fraction and velocity fields, and are expected to play a crucial role during the ignition process. Furthermore, profiles for the mean and RMS velocity components predicted by the CFD model have been compared against those obtained through experimental observations, showing good agreement. Therefore, this investigation and the derived methodology for defining a meshing strategy provides a suitable background for further studies on modelling the atomization phenomena associated to liquid fuel injections.

Acknowledgements

This work was partly sponsored by the program “Ayuda a Primeros Proyectos de Investigación (PAID-06-18), Vicerrectorado de Investigación, Innovación y Transferencia de la Universitat Politècnica de València (UPV), Spain”. We thankfully acknowledge the computer resources at Altamira Supercomputer and the technical support provided by Universidad de Cantabria (RES FI-2018-1-0012 and FI-2018-2-0029) in the frame of the Spanish Supercomputing Network. On the other hand, the support given to Mr Mario Belmar by Universitat Politècnica de València through the “FPI-Subprograma 2” grant within the “Programa de Apoyo para la Investigación y Desarrollo (PAID-01-18)” is gratefully acknowledged.

Nomenclature

D	external swirl cup exit diameter [m]
NMSE	Normalized Mean Square Error [-]
p	pressure [bar]
R	radius of injection [m]
S	swirl number [-]
T	temperature [K]
u	axial velocity component [m s^{-1}]
w	tangential velocity component [m s^{-1}]
y^+	non-dimensional distance to the wall [-]
Z	fuel mass fraction [-]
ϕ	value of a given flow variable

References

[1] Madden, P. Jul. 2. 2011, FORUM-AE.
[2] Lefebvre, A. H., 1998, “Gas turbine combustion”.
[3] Ramaekers, W., Tap, F., Boersma, B., 2018, Turbulence and Combustion, 100(2), pp. 457–479.
[4] Menon, S., Patel, N., 2006, The American Institute of Aeronautics and Astronautics Journal, 44(4), 709–723.
[5] Tacina, K. M., Chang, C., He, Z. J., Lee, P., Mongia, H. C., Dam, B. K. Jul. 28.-30. 2014, 50th AIAA/ASME/SAE/ASEE Joint Propulsion Conference.
[6] Marrero-Santiago, J., Verdier, A., Godard, G., Vandel, A., Cabot, G., Boukhalfa, A. M., Renou, B., Sep. 4.-7. 2016, 27th European Conference on Liquid Atomization and Spray Systems.
[7] Reddemann, M.A., Mathieu, F. Kneer, R., 2013, Experiments in Fluids, 54(11).
[8] Wey, T., Liu, N.-S., Jan. 9.-12. 2012, 50th Aerospace Sciences Meeting and Exhibit (AIAA).
[9] Moureau, V., Domingo, P., Vervisch, L., 2011, Combustion and Flame, 158(7), pp. 1340–1357.
[10] Kırtaş M, Patel N., Sankaran V. Menon S., May 8.-11. 2006, Proceedings Turbo Expo (ASME).
[11] Hasti, V. R., Kundu, P., Kumar, G., Drennan, S. A., Som, S., Gore, J., Jun. 9.-11. 2018, AIAA/ASME/SAE/ASEE Joint Propulsion Conference.
[12] Esclapez, L., Riber, E., Cuenot, B., 2015, Proceedings of the Combustion Institute, 35 (3), pp. 3133–3141.
[13] Convergent Science, 2017, “CONVERGE 2.4 Manual”.
[14] Hanna, S., Hansen, O., Dharmavaram, S., 2004, Atmospheric Environment, 38(28), pp. 4675–4687.
[15] Huang, Y., Yang, V., 2009, Progress in Energy and Combustion Science, 35(4), pp. 293–364.
[16] Syred, N., Beér, J. M., 1974, Combustion and Flame, 23(2), pp. 143–201.
[17] Pope, S. B., 2000, “Turbulent Flows”.
[18] Tacina, R., Cai, J., Jeng, S.-M., Jan. 10.-13. 2005, 43rd AIAA Aerospace Sciences Meeting & Exhibit.